Properties of polylactide inks for solvent-cast printing of three-dimensional freeform microstructures

Shuang-Zhuang Guo[1], Marie-Claude Heuzey[2] and Daniel Therriault[1]

[1] Laboratory of Multiscale Mechanics, Mechanical Engineering Department

Center for Applied Research on Polymers and composites (CREPEC)

École Polytechnique de Montréal, C.P. 6079, succ. Centre-Ville,

Montreal, QC H3C 3A7 (Canada)

[2] Chemical Engineering Department

Center for Applied Research on Polymers and composites (CREPEC)

École Polytechnique de Montréal, C.P. 6079, succ. Centre-Ville,

Montreal, QC H3C 3A7 (Canada) E-mail: marie-claude.heuzey@polymtl.ca

KEYWORDS: Polylactide, solvent-cast, 3D printing, rheology, crystallization, microfabrication

ABSTRACT

Solvent-cast printing is a highly versatile microfabrication technique that can be used to construct various geometries such as filaments, towers, scaffolds and freeform circular spirals by the robotic deposition of a polymer solution ink onto a moving stage. In this work, we have performed a comprehensive characterization of the solvent-cast printing process using polylactide (PLA) solutions by analyzing the flow behavior of the solutions, the solvent evaporation kinetics and the effect of process-related parameters on the crystallization of the extruded filaments. Rotational rheometry at low to moderate shear rates showed a nearly Newtonian behavior of the PLA solutions, while capillary flow analysis based on process-related data indicated shear-thinning at high shear rates. Solvent vaporization tests suggested that the internal diffusion of the solvent through the filaments controlled the solvent removal of the extrudates. Different kinds of three-dimensional (3D) structures including a layer-by-layer tower, 9-layer scaffold and freeform spiral were fabricated, and a processing map was given to show the proper ranges of process-related parameters (*i.e.*, polymer content, applied pressure, nozzle diameter and robot velocity) for the different geometries. The results of differential scanning calorimetry revealed that slow solvent evaporation could increase the ability of PLA to complete its crystallization process during the filament drying stage. The method developed here offers a new perspective for manufacturing complex structures from polymer solutions and provide guidelines to optimize the various parameters for 3D geometry fabrication.

Introduction

There is a growing interest towards the fabrication of three-dimensional (3D) micro or nanoscale devices made from thermoset[1], or thermoplastic polymers[2], hydrogels[3-4], or polyelectrolytes[5], which may find potential applications in complex microfluidic networks[6-7], tissue engineering scaffolds[8-9], and self-supporting sensors[10-11]. Several strategies have been employed to precisely assemble 3D structures, including photolithographic[12], colloidal-epitaxy[13] and direct-write techniques[14-15]. Among these, the direct-write assembly is one of the most promising approaches because it offers flexibility in material selection, low cost, and ability to construct complex 3D structures[16]. Direct-write assembly is a 3D printing technique, which employs a computer-controlled translational stage that moves a pattern-generating device in order to achieve, layer by layer, the desired 3D microstructure[17]. Different materials such as organic fugitive[7, 15, 18-20] or colloidal inks[21-23], concentrated polyelectrolytes[24-25], UV curable thermosets[1, 10] and bioinks (*e.g.* hydrogels with suspended cells)[26-28] , have been employed in this technique to fabricate various micro structures for specific applications.

Polylactide (PLA) is one of the most popular bio-based thermoplastic materials because it is widely available commercially, biodegradable, biocompatible and has a relative high-strength, high-modulus and good processability[29-31]. A few techniques using PLA to fabricate microscale 3D geometries have been developed and described in the literature. For example, a fused deposition modeling (FDM) method can create PLA solid objects with ~250 μm resolution due to the material rigidity increase after

the temperature-triggered phase transition from molten to solid state[32]. However this method exhibits limited precision of the printed features, and the high viscosity and/or thermal degradation at high temperature of thermoplastic melts may restrict this approach. In addition, two other methods including surface tension driven direct-write[33] and soft lithographic approaches[34] were reported to fabricate 3D PLA scaffolds for tissue engineering. However, these techniques were unable to build complex or freeform 3D structures.

We recently reported the solvent-cast direct-write printing of 3D geometries in a freeform fashion using concentrated PLA solution inks[35] as illustrated in Figure 1. Specifically, the inks are formulated by dissolving PLA in a solvent with low boiling point. The resulting solutions are extruded through micronozzles upon the application of an appropriate pressure. They rapidly undergo fluid-like to solid-like transition post-extrusion due to fast solvent evaporation, which allows maintaining their filamentary shape and buildup of complex structures. Mechanical and electrical properties under functional testing of some of the constructs fabricated are reported in reference 35.

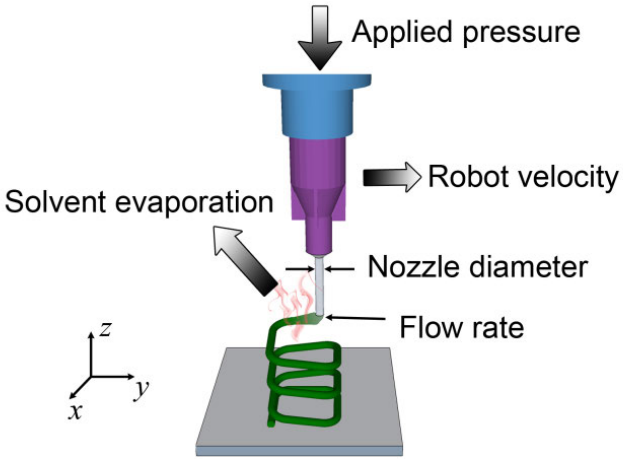

Figure 1. Schematic of the solvent-cast printing process and the main process parameters.

In this paper, we present a comprehensive study of the properties of PLA solution inks for the solvent-cast printing method. The information gathered here aims at elucidating the phase behavior and rheological properties of the inks during the solvent-cast printing process, and can be used as a guide for the fabrication of different 2D and 3D geometries. The process-related viscosity of PLA solutions is investigated by capillary flow analysis. The solvent evaporation kinetics are characterized by monitoring the weight reduction of short extruded filaments over time. In addition, a map of processing parameters ranges for different microstructure fabrication is proposed. Finally, the crystallization properties of the extrudates are examined using a differential scanning calorimetry (DSC).

Experimental Section

Polymer Solution Preparation

A semi-crystalline polylactide (PLA, grade 4032D, Nature works LLC) with a stereoisomer composition of 1.2-1.6% *D*-isomer lactide, was used in this study. Various amount of neat PLA (20, 25 and 30 wt% solutions) were dissolved in the solvent dichloromethane (DCM, Sigma-Aldrich). After 24 h, the solutions were ultrasonicated (ultrasonic cleaner 8891, Cole-Parmer) at 42 kHz for 1 h. Then the polymer solutions were stored in sealed bottles until processing.

3D Printing

The solvent-cast printing was performed using a moving stage along the *x*-axis and a robot head (I&J2200-4, I&J Fisnar) moving in the *y-z* plane that were computer-controlled with commercial software (JR Points for Dispensing, Janome Sewing Machine). The PLA solution was poured in a syringe (3cc barrel, EFD) fixed on the robot and deposited through a micronozzle onto a glass substrate at room temperature. The pressure applied on the polymer solution (0 to 4.2 MPa) was controlled by an air-powered dispensing system (HP-7X, EFD). This experimental set-up was also used in the capillary flow analysis, the solvent evaporation tests and the fabrication of the different geometries.

Rheological Characterization

The process related viscosities of polymer solutions with various PLA contents (20, 25, 30 wt%) were evaluated from constant-pressure capillary flow analysis as described in[20]. The different PLA solutions were extruded through a single size micronozzle (inner diameter D = 200 µm, capillary length L = 12.24 mm) and the 25 wt% PLA solution was also extruded through two other nozzles (D = 100 and 330 µm, L = 12.76 and 12.24 mm). The high-capacity pressure dispenser was set between 0.18 and 4.0 MPa to obtain the desired flow rate, depending on the PLA content and nozzle diameter. After reaching the extrusion steady state, the ink was deposited onto a substrate for 120 s under various applied pressures at a robot velocity 0.5 mm s^{-1}. After drying in an oven (G05053-10, Cole-Parmer) at 50°C for 12 h, the extruded fibers were then weighed with a high precision balance (GH-202, A&D Engineering) to determine the mass flow rates, which were converted to volumetric flow rates using

the respective fluid densities. Capillary data reported in this work include the Rabinowitch-Mooney correction for non-Newtonian fluids.

The steady-state shear viscosity of the polymer solutions was also characterized at room temperature using a rotational rheometer (MCR-502, Anton Paar) with a pressure flow cell (CC25 concentric cylinder geometry) to prevent solvent evaporation. The shear rate ramp started from 0.1 s^{-1} and increased until flow instabilities were observed at $\sim$ 100 s^{-1}, where the viscosity dramatically decreased. Each polymer solution was tested under ambient pressure and three different applied cell pressures (1.0, 2.0 and 4.0 MPa).

Solvent Evaporation Rate Characterization

The solvent evaporation behavior of the polymer inks was evaluated by directly depositing a 5 mm-long filament on a glass substrate resting on a high-precision balance (GH-202, A&D Engineering). Three polymer solutions (PLA contents of 20, 25 and 30 wt%) were deposited on the substrates for 5 s through a micronozzle (D = 510 μm), under an applied pressure of 420 kPa. The 20 wt% PLA solution was also deposited using two other nozzles (D = 200 and 330 μm). The sample weight was recorded for 6 h. Following this recording period, the sample was completely dried in an oven (G05053-10, Cole-Parmer) at 50ºC for 12 h and weighed again. The mass of the dried PLA was then used to calculate the real-time solvent percentage in the extruded filament.

Microstructure Fabrication

2D and 3D microstructures were fabricated using the solvent-cast printing technique. A nine-layer scaffold was fabricated with the 25 wt% PLA solution using a 100 μm inner diameter nozzle under an applied pressure of 1.4 MPa and 1.0 mm s^{-1} robot velocity. Square and circular towers were built with the 30 wt% PLA solution using a nozzle with a 200 μm inner diameter under an applied pressure of 1.05 MPa and 0.5 mm s^{-1} robot velocity. A 3D circular spiral was fabricated from the 30 wt% PLA solution using a micronozzle with a 100 μm inner diameter under an applied pressure of 1.75 MPa and 0.1 mm s^{-1} robot velocity. The designed pitch of the circular spiral and the radius of the coil were 0.5 mm.

Morphological Characterization

The morphology of the various microstructures was observed on a JEOL JSM-840 Scanning Electron Microscope (SEM). Samples were sputtered with gold for 15 s prior to the imaging.

Thermal Analysis

Critical transition temperatures and extent of crystallization of the printed PLA filaments were determined using differential scanning calorimetry (DSC Q1000, TA Instruments) in a nitrogen atmosphere. Ten samples were prepared by depositing PLA filaments using different process parameters. Details of the various experiments are provided in Table 1 where, for example, the nomenclature of 20%/200μm/1.05MPa/0.5mms^{-1} represents a filament specimen fabricated using the 20 wt% PLA solution, 200 μm inner diameter nozzle, 1.05 MPa applied pressure and

0.5 mm s^{-1} robot velocity. After drying the printed filaments in an oven at 50ºC for 12 h, the samples were cut and placed in sealed aluminum pans. For each sample, the heat flow measurements were performed during a heating from 30 to 210ºC at a heating rate of 10ºC min^{-1}. The glass transition temperature (T_g), cold crystallization temperature (T_{cc}), melting temperature (T_m), and degree of crystallinity (χ_c) were determined from the measured thermograms.

Table 1. DSC results of solvent-cast PLA filament crystallization

Sample nomenclature *	ΔH_m (J g^{-1})	ΔH_{cc} (J g^{-1})	$\Delta H_{\alpha' \to \alpha}$ (J g^{-1})	χ_c (%)
20%/200μm/1.05MPa/0.5mms^{-1}	36.8	16.3	0.73	21.1
25%/200μm/0.56MPa/0.5mms^{-1}	32.3	23.8	0.90	8.1
25%/200μm/1.05MPa/0.5mms^{-1}	35.1	15.9	0.59	19.9
25%/200μm/1.05MPa/0.2mms^{-1}	32.1	4.9	0.00	29.0
25%/200μm/1.05MPa/1.0mms^{-1}	34.9	24.8	0.72	10.1
25%/200μm/1.05MPa/2.0mms^{-1}	29.2	21.5	0.83	7.3
25%/200μm/2.84MPa/0.5mms^{-1}	34.0	2.7	0.00	33.4
25%/100μm/1.05MPa/0.5mms^{-1}	31.0	18.9	1.29	11.5
25%/330μm/1.05MPa/0.5mms^{-1}	35.3	2.0	0.00	35.5
30%/200μm/1.05MPa/0.5mms^{-1}	35.3	17.0	0.71	18.8

* nomenclature: PLA content/nozzle diameter/applied pressure/robot velocity

Results and Discussion

Rheological Properties

This printing process involves the flow of a polymer solution inside a nozzle, hence rheological properties of the solution inks are critical. The solution must exhibit a moderate viscosity, so it can flow easily through the fine nozzle and result in a stable filament. Since polymer solutions exhibit high viscosity, a shear-shinning behavior of the extruded material is favorable. The flow behavior of various PLA solutions under two different operating conditions (*i.e.*, nozzle diameter and applied pressure) was examined using capillary flow analysis from the process related raw data, as explained below. Figure 2 shows the volumetric flow rate converted from mass flow rate with respect to the applied pressure. For all PLA solutions investigated, the flow rate increased with the applied pressure, as expected. Under the same pressure, the flow rate decreased as the PLA content increased (Figure 2a) and as the nozzle diameter decreased (Figure 2b).

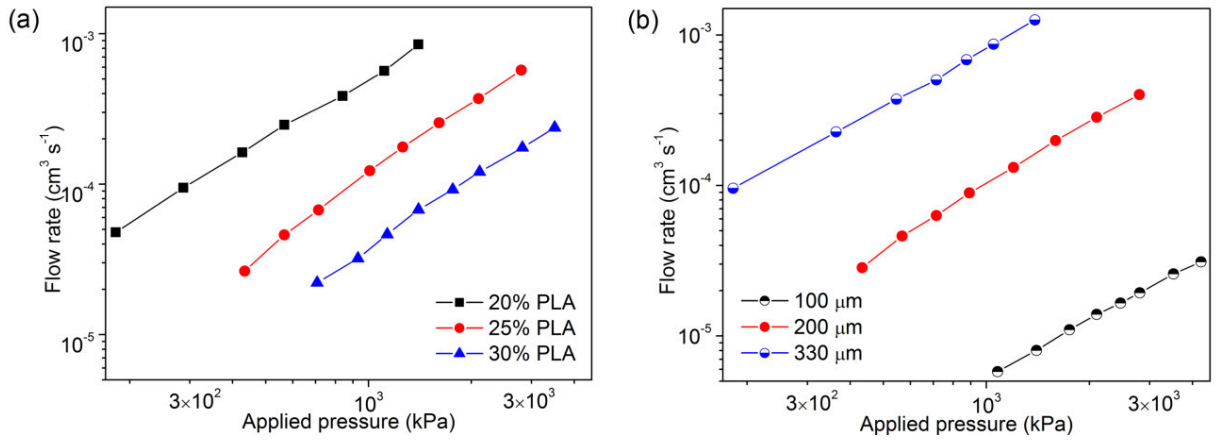

Figure 2. Raw data of the capillary flow experiments: volumetric flow rate as a function of the applied pressure for (a) three PLA solutions (20, 25 and 30 wt%)

deposited using a 200 μm nozzle, and (b) a 25 wt% PLA solution deposited using three different nozzle diameters (100, 200 and 330 μm).

Because the ratio of micronozzle length (L) to diameter (D) is larger than 50, the end effects in the capillary flow analysis was neglected[20]. It is also assumed that the pressure has negligible effect on the viscosity. The process-related wall shear stress τ_w is calculated from the following equation:

$$\tau_w = \Delta P \cdot R/2L \quad (1)$$

where ΔP is the applied pressure during the process, and R is the nozzle inner radius. The wall shear rate $\dot{\gamma}_w$ is determined from the volumetric flow rate Q, by first calculating the Newtonian shear rate $\dot{\gamma}_{Newt}$:

$$\dot{\gamma}_{Newt} = 4Q/\pi R^3 \quad (2)$$

and correcting for non-Newtonian effects using

$$\dot{\gamma}_w = \dot{\gamma}_{Newt}\,(3n+1)/4n \quad (3)$$

where the bracketed term is the Rabinowitch-Mooney correction. The parameter n is defined by

$$n = d\log(\tau_w)/d\log(\dot{\gamma}_w) \quad (4)$$

which can be determined from the slope of the log-log plot of τ_w versus $\dot{\gamma}_{Newt}$. Therefore with Equation (3) that represents the process-related shear rate, the apparent viscosity of the polymer solution can be determined from:

$$\eta_{app} = \tau_w/\dot{\gamma}_W \quad (5)$$

The solid symbols in Figure 3 represent the apparent process viscosity as a function of the process-related shear rate $\dot{\gamma}_w$ for three different solutions (*i.e.*, 20, 25 and 30 wt% PLA content), calculated from the capillary flow data obtained using a nozzle diameter of 200 μm. The three PLA solutions exhibited a shear-thinning behavior over the investigated shear rates. The lower shear rate limit was attributed to the balance precision used to determine the mass flow rate. This lower limit decreased as the PLA content increased. In addition, the results of apparent viscosity as a function of the process-related shear rate for the 25 wt% PLA solution for two other nozzle diameters (*i.e.*, 100 and 330 μm) (not shown here) indicated no specific dependence of the apparent viscosity on nozzle size, hence no obvious wall effects.

The open symbols in Figure 3 show the viscosities of the three PLA solutions (*i.e.*, 20, 25 and 30 wt%) as functions of shear rate, measured in rotational rheometry under ambient pressure and steady simple shear. The three PLA solutions exhibited a Newtonian behavior over the range of low to moderate shear rates ($\sim$ 2 - 80 s^{-1}) allowable during the rotational rheometry tests. The upper limitation of achievable high shear rate was due to flow instabilities of the polymer solutions, where the viscosities sharply decreased. The upper limit of shear rate increased slightly as the PLA content decreased from 30 wt% to 20 wt% because the latter is less elastic. In addition, the flow behavior of the three PLA solutions under different applied pressures (1.0, 2.0 and 4.0 MPa) was nearly the same (not shown here), which demonstrated that the pressure range used in the fabricating process had negligible effect on the ink's viscosity. The rotational rheometry and process-related data agree

reasonably well, showing a bimodal behavior from a nearly Newtonian regime followed by a significant power-law drop. The rheological measurements also revealed that the viscosity of PLA solutions was greatly affected by PLA content. Under the same shear rate, the viscosity of the 30 wt% PLA solution was almost one order of magnitude superior to that of the 20 wt% PLA solution.

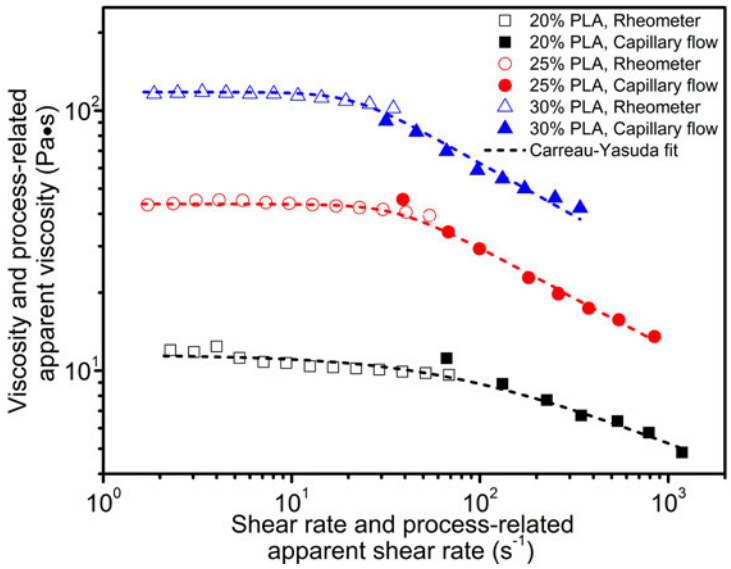

Figure 3. Viscosity as a function of shear rate for three PLA solutions. (open symbols: data obtained using a concentric cylinder flow geometry in steady simple shear, solid symbols: data obtained by extrusion of the PLA solutions with a 200 μm nozzle in capillary flow analysis, dash lines: fits of Carreau-Yasuda model with parameters of the fit given in Table 2).

The dash lines in Figure 3 represent the fits of the Carreau-Yasuda model, which is quite flexible in fitting the non-Newtonian behavior of $\eta(\dot{\gamma})$ over a wide range of shear rate, and is expressed as follows

$$\frac{\eta-\eta_\infty}{\eta_0-\eta_\infty} = [1 + |t_1\dot{\gamma}|^a]^{(n-1)/a} \quad (6)$$

where η_0 is the zero-shear-rate viscosity, η_∞ is the infinite-shear-rate viscosity, t_1 is a critical time constant, (n-1) is the power law exponent, and a is a dimensionless parameter that describes the width of the transition between the zero-shear-rate and power-law regions. For polymer solutions, $\eta_\infty \approx 0$. The fitting parameters of Equation (6) for the curves superimposed on the experimental data of Figure 3 are given in Table 2. The relatively good fit of the Carreau-Yasuda model confirms that the calculation of the viscosity from the process-related data gives quite reasonable values. The η_0 values increase with PLA content, as expected, and the transition from Newtonian to power-law regime is shifted to lower shear rates. The shear-thinning character also increases with PLA concentration (lower n). The parameters listed in Table 2 may be useful for further modeling purposes of the printing process.

Table 2. Parameter values of the Carreau-Yasuda model fit for the PLA solutions (data from Figure 3).

PLA content (wt%)	$\boldsymbol{\eta_0}$ (Pa • s)	t_1 (s)	a –	n –	*Adj. R²* –
20	11.5	0.014	1.00	0.71	0.95
25	43.6	0.028	3.15	0.62	0.98
30	118	0.047	3.36	0.59	0.98

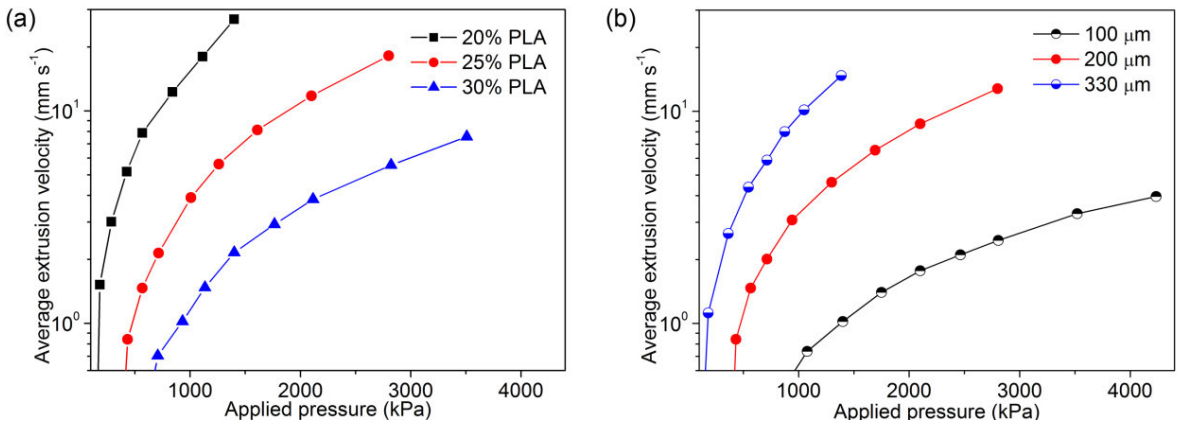

Figure 4. Average extrusion velocity as a function of applied pressure for (a) different PLA solutions (20, 25 and 30 wt%) deposited using a 200 µm nozzle, and (b) a 25 wt% PLA solution deposited using three different nozzle diameters (100, 200 and 330 µm) (data from Figure 2).

Figure 4 presents the calculated average material extrusion velocity as a function of the applied pressure for the same PLA contents extruded from a nozzle diameter of 200 µm (Figure 4a), and for the 25 wt% PLA solution extruded from different nozzle diameters (100, 200 and 330 µm) (Figure 4b). The velocity data were calculated from the raw volumetric flow rate data (Figure 2) divided by the nozzle cross-sectional area. These plots are important to set the fabrication parameters for successful 3D printing, by adjusting the pressure of the dispenser system with the corresponding robot velocity for various inks and nozzle sizes. The polymer solutions exhibited different flow behaviors where higher PLA contents led to higher viscosities and hence lower average velocities (Figure 4a). Moreover, larger nozzle diameters caused higher average velocities for the same PLA solution (Figure 4b). At the same pressure, the average extrusion velocity from the 330 µm nozzle was approximately

ten times that of the 100 μm nozzle. In addition, the extrapolation of the velocity curves toward low pressures shows a minimum pressure required for flow, as observed during the printing process. This minimum pressure may have similarity with the concept of yield stress, though this is not expected from a polymer solution and is most likely inherent to the process itself.

Solvent Evaporation Rate

After the filament extrusion from the micronozzle, the solvent evaporation plays a crucial role in the phase change from solution to solid to guarantee geometric retention. There are three mechanisms of solvent removal from the extruded filament: 1) flash vaporization, 2) diffusion within the filament, and 3) convective transfer from the filament surface to the surrounding air[36-38]. Flash vaporization takes place near the nozzle tip due to a high pressure drop after the filament extrusion. Next, the solvent molecules must diffuse through the filament (internal diffusion) in order to evaporate at the air/filament interface (external convection). In this work, the solvent evaporation behavior was investigated by monitoring the weight reduction of deposited filaments as a function of time using a high-precision balance. Figure 5a shows the evolution with time of the normalized solvent content (divided by the solvent content at the measurement starting point) for short filaments (length of $\sim$ 5 mm) deposited using three different PLA solutions (20, 25 and 30 wt%) through a 510 μm inner diameter nozzle. Since there were initial fluctuations of the balance readings during the first 10 s, the mechanism of flash vaporization was not adequately captured during the experiments and is not reported. For the filaments extruded using different

PLA solutions, the plots of normalized solvent content versus time had no distinct difference (Figure 5a). In other words, the initial solvent contents had no obvious effects on the solvent internal diffusion, which was also shown by N. Kojić *et al*[39]. However, when raw evaporation data is examined[35] (*i.e.*, not normalized), the most concentrated PLA solution is the one that solidifies the fastest. Figure 5b displays the normalized evaporation data for filaments extruded using the 20 wt% PLA solution through different nozzle diameters (200, 330 and 510 μm). The solvent evaporation rate significantly increased as the filament diameter decreased, because the solvent internal diffusion was greatly accelerated by shortening the diffusion distance. From the results of Figure 5, it seems that the internal diffusion of the solvent through the filament is the governing process for the solvent removal of the extrudates. In other words, the smaller the extruded filament is, the faster does its rigidity increase.

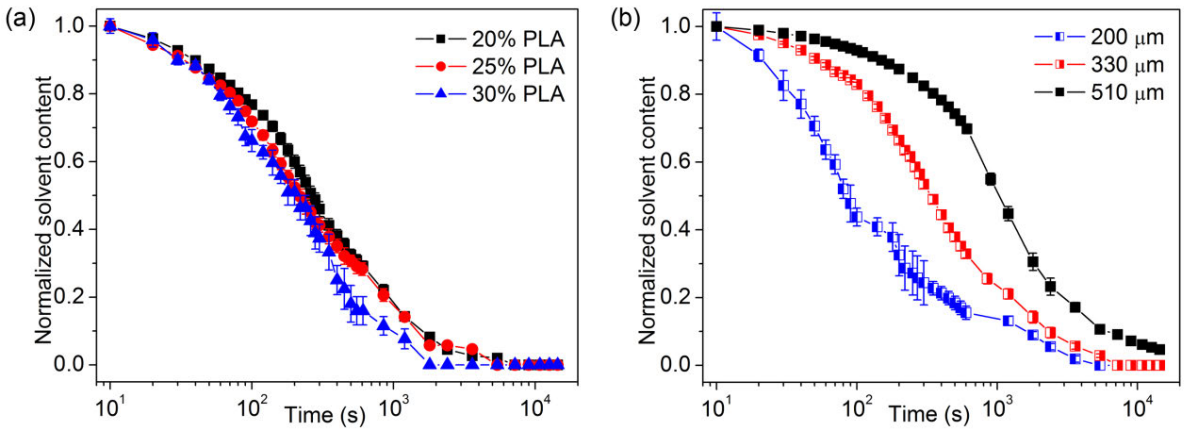

Figure 5. Normalized solvent content as a function of time for (a) three 5 mm long PLA filaments deposited using a 510 μm nozzle under 0.42 MPa applied pressure and 1 mm s^{-1} robot velocity, and (b) 20 wt% PLA solution deposited using three different nozzles under 0.42 MPa applied pressure and 1 mm s^{-1} robot velocity for 5 s.

Microstructure Fabrication

The four main printing parameters in this work are PLA content, applied pressure, nozzle diameter, and robot velocity, which greatly affect the diameter of the extruded filament and the solvent evaporation rate (corresponding to filament rigidity increase). The fastest solvent evaporation could be achieved by either increasing the PLA content[35] or the robot velocity, or by either decreasing the applied pressure or the nozzle diameter. The applied pressure and robot velocity can be appropriately set from 0 to 4.2 MPa, and from 0.1 to 500 mm s^{-1} respectively, guided by the rheological data shown in Figure 4 and trial error. Three PLA solutions (PLA content of 20, 25 and 30 wt%) and six nozzles (D = 100, 150, 200, 250, 330 and 510 μm) were used in this process mapping. The successful fabrication of different geometries (*e.g.*, 1D filament, 2D network, 3D layer-by-layer and freeform structure) required different solidification speeds, hence different solvent evaporation rates, formulations and operating conditions. Figure 6 shows a processing map with approximate ranges of PLA content and nozzle diameter for the fabrication of different geometries. Zone I in Figure 6 indicates that a 1D filament could be easily fabricated using a wide range of parameters values. As part of Zone I, Zone II reveals that the fabrication of a 2D network or a 3D layer-by-layer structure needed faster solvent evaporation rate, which meant a narrower range of parameter values. Moreover, to fabricate 3D freeform structures, the solvent must evaporate much faster so that the geometry exhibits enough rigidity to support itself right after extrusion. Therefore, Zone III indicates that successful 3D freeform fabrication could only be achieved using much smaller

nozzles and the more viscous PLA solutions. In addition, Zone IV displays that it was difficult to fabricate continuous and smooth filament using larger nozzle diameters. Finally, Zone V indicates that PLA was insoluble in DCM at high content (> 32%), and Zone VI shows that more dilute PLA solutions could be used in solvent-cast printing.

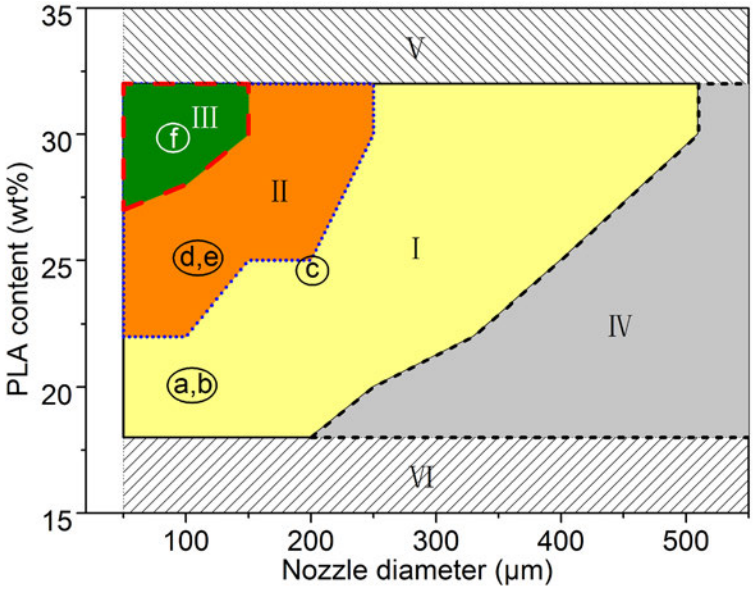

Figure 6. Solvent-cast printing processing map showing the parameter ranges for different microstructures fabrication. I. zone for 1D filament, II. zone for 2D filament array or 3D layer-by-layer structure, III. zone for 3D freeform geometry, IV. zone where filaments break, V. zone where PLA is not dissolvable, VI. zone where PLA solutions are too dilute for the process. The letters a-f represent the fabrication parameters of different geometries shown in Figure 7.

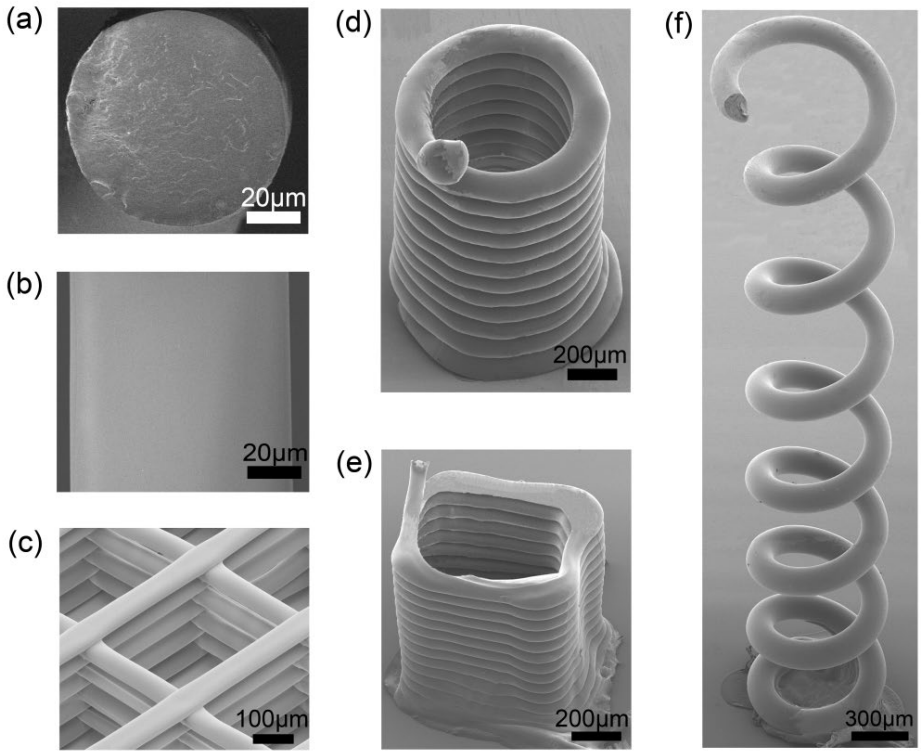

Figure 7. Morphology of various printed microstructures. (a) Representative SEM image of the PLA filament circular cross section. (b) Representative SEM image of the filament smooth surface. (c) Inclined top view SEM image of PLA 9-layer scaffold. (d) SEM image of a PLA circular tower. (e) SEM image of a PLA square tower. (f) Inclined top view SEM image of a PLA circular spiral.

Various geometries with different dimensions were printed using the right conditions indicated in Figure 6. Figure 7a shows SEM images of a typical filament circular cross-section with a diameter of ～ 100 μm, which was fabricated with the 20 wt% PLA solution using a 100 μm inner diameter nozzle, under an applied pressure of 0.4 MPa and 1.0 mm s^{-1} robot velocity. Figure 7b displays a close-up view of the relatively smooth surface of the PLA filament. Figure 7c reveals a scaffold consisting of nine 2D filament layers, which was fabricated with the 25 wt% PLA

solution using a 100 μm inner diameter nozzle, under an applied pressure of 1.4 MPa and 1.0 mm s^{-1} robot velocity. The scaffold was almost identical to its programmed deposition paths because the printing layer was always supported by the underlying layer. Figure 7d,e show 3D circular and square towers, which were built with the 25 wt% PLA solution using a nozzle with a 100 μm inner diameter, under an applied pressure of 1.05 MPa and 0.2 mm s^{-1} robot velocity. The circular tower had 1.0 mm diameter and 1.5 mm height, while the square tower had 1.0 mm side length and 1.5 mm height. Finally, Figure 7f presents a 3D freeform helical microstructure, which was fabricated with the 30 wt% PLA solution using a micronozzle with a 100 μm inner diameter, under an applied pressure of 1.75 MPa and 0.1 mm s^{-1} robot velocity. The pitch of the circular spiral was 0.5 mm and the radius of the coil was 0.5 mm. Consequently, the solvent-cast printing method was demonstrated to be a flexible micromanufacturing process to fabricate unique structures, giving that the process and material parameters are correctly selected. These more complex structures are generally difficult to produce by conventional single-stage processing methods.

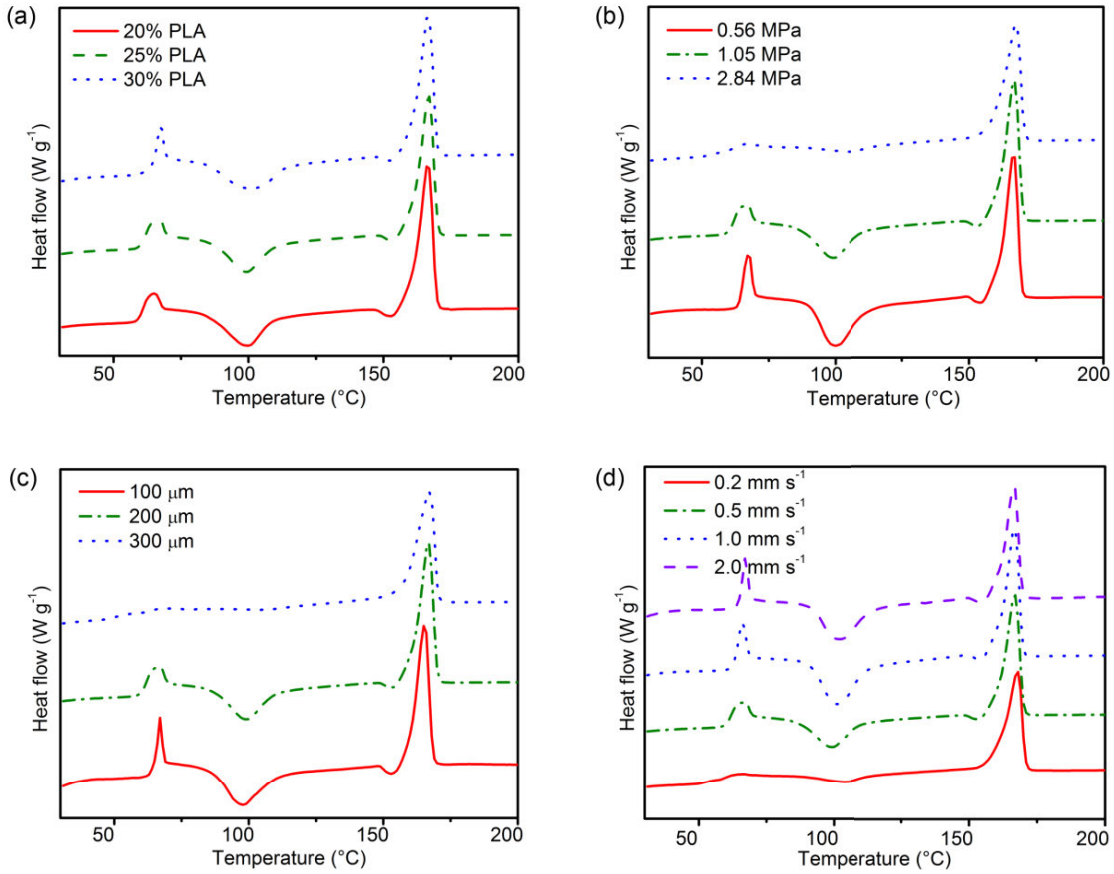

Figure 8. DSC thermogram of PLA filaments obtained at a heating rate of 10ºC min^{-1} for different printing parameters: (a) PLA content, (b) applied pressure, (c) nozzle diameter, and (d) robot velocity.

Thermal and Crystallization Analysis

The thermal, mechanical and barrier properties of PLA are dependent on its crystalline structure and content, which are largely determined by the processing parameters[40-41]. DSC experiments were carried out to investigate the crystallization behavior of PLA filaments fabricated under various operating conditions within the range shown in Figure 6 for successful printing. Figure 8 shows the effects of the four

main process parameters (*i.e.*, PLA content, applied pressure, nozzle diameter and robot velocity) on the heat flow recorded during a temperature sweep on different PLA filaments. All heat flow curves show peaks representing the glass transition (T_g), cold crystallization (T_{cc}) and melting (T_m) temperatures at approximately 65ºC, 100ºC and 166ºC, respectively. Since the T_g and T_m of PLA are strongly dependent on both the molecular weight and the optical purity (*i.e.*, fraction of the *L*-isomer lactide) of the polymer, the four process parameters had no significant effects on T_g and T_m within the range investigated. In addition, for the curves exhibiting cold crystallization at 100ºC, a small exothermic peak (denoted as T_{exo}) prior to the melting peak was observed at 153ºC, which is generally attributed to a transformation of the crystalline phase from the disordered α′ structure to the ordered α structure[40, 42]. For PLA content between 20 and 30 wt%, the thermograms obtained show similar trends (Figure 8a). Increasing the applied pressure from 0.56 to 2.84 MPa, the peak of cold crystallization decreased to nearly disappearing (Figure 8b). Similar evolution of cold crystallization was observed when the nozzle diameter changed from 100 to 330 μm, or the robot velocity decreased from 2.0 to 0.2 mm s^{-1} (Figure 8c,d). This might be due to the fact that larger applied pressure, thicker nozzle or smaller robot velocity lead to thicker filaments, which could result in lower solvent evaporation rate (Figure 5b) and consequently more time for polymer chains to rearrange in crystalline domains.

Table 1 shows the crystallization data of PLA filaments calculated from the DSC results. The melting enthalpy of the total crystalline phase (ΔH_m) corresponds to the

sum of the melting enthalpies of the original crystalline phase (ΔH_{mc}) and the crystallized phase during the DSC test, including cold crystallization (ΔH_{cc}) and α′-to-α phase transition ($\Delta H_{\alpha' \to \alpha}$)[42-43]. Crystallinity of the original PLA filament (χ_c), therefore, was estimated using the following equation:

$$\chi_c = \frac{\Delta H_m - \Delta H_{cc} - \Delta H_{\alpha' \to \alpha}}{\Delta H_m^0} \times 100 \quad (6)$$

where ΔH_m^0 (93.6 J g^{-1}) is the enthalpy of fusion of 100% crystalline PLA[44-45]. Figure 9 shows the comparison of the crystallinity of the PLA filaments manufactured under different conditions. For the filaments made from various PLA contents but using the same processing conditions, the values of crystallinity were nearly the same (Figure 9a), which agrees with the results of the normalized solvent evaporation rates shown in Figure 5a. This may be attributed to the fact that similar solvent evaporation time results in equivalent crystallinity evolution for the different PLA solutions. In addition, as seen in Figure 9(b-d), the crystallinity was significantly enhanced by increasing the applied pressure and nozzle diameter, or decreasing the robot velocity. These results are in agreement with the variation of the cold crystallization peak shown in Figure 8. The higher crystallinity the original filament had, the smaller cold crystallization peak in the thermogram was. Therefore, wise choice of operating conditions and ink formulation may determine the ability of PLA to complete the crystallization process during the printing stage. Furthermore, the properties of PLA structures such as heat resistance, tensile strength and barrier that benefit from high crystallization may be tuned according to the application requirements.

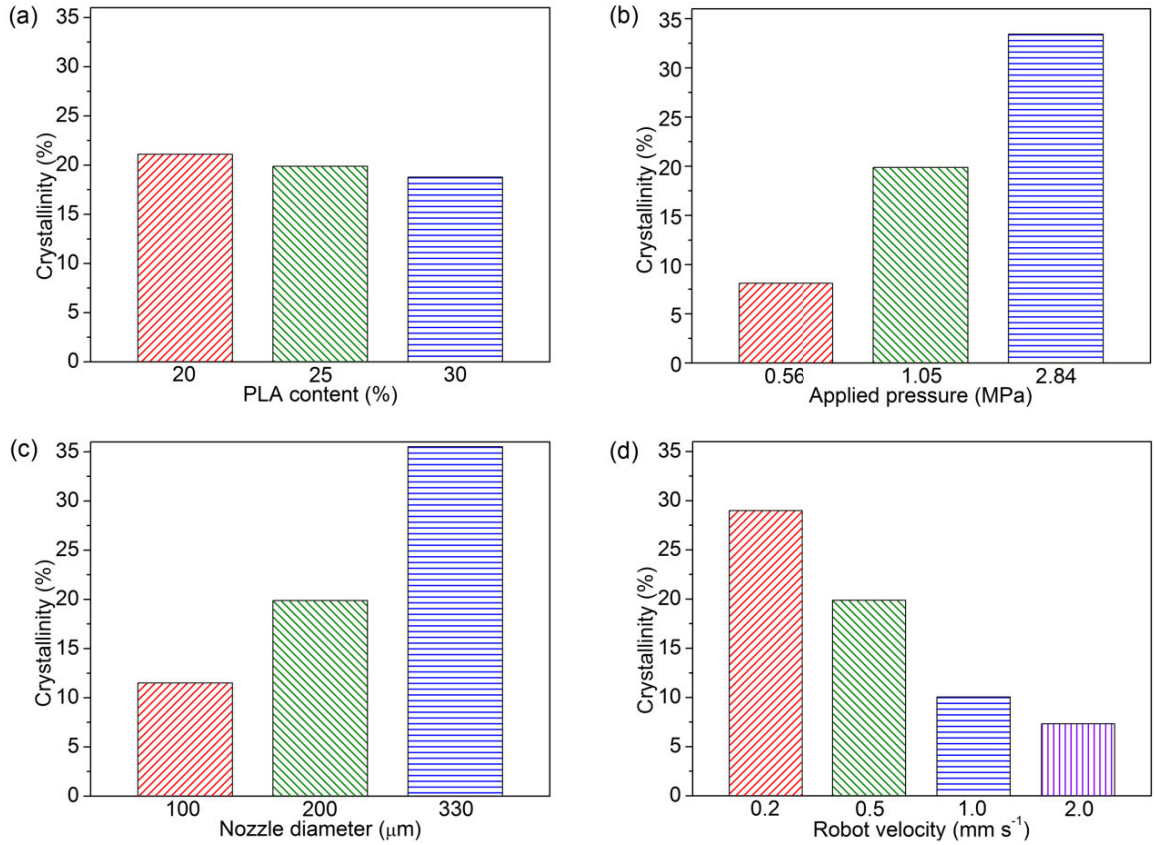

Figure 9. Effects of different printing parameters: (a) PLA content in solution, (b) applied pressure, (c) nozzle diameter, (d) robot velocity on the crystallinity of PLA filaments. The data and process parameters are list in Table 1.

Conclusions

In this work, the process of solvent-cast 3D printing of PLA solutions was thoroughly investigated. Parameters such as ink rheological properties, solidification kinetics, operating conditions, and crystallinity of microstructures were examined. The PLA solutions behaved as shear-shinning fluids inside the nozzle and the process apparent viscosity was greatly dependent on the polymer content. Faster solvent

evaporation could be achieved by decreasing the diameter of extrudates, which could be realized by increasing the robot velocity, or decreasing the applied pressure and nozzle diameter. However, higher crystallization of the extruded geometries could benefit from the slower solvent evaporation. As the fabrication complexity of micro geometries evolves from 1D filament, 2D fiber array to 3D scaffold and freeform spiral, the rigidity of the filament needs to increase faster as well. Thus the processing map for the most complex geometry gets narrower. The results presented in this work provide a useful insight on the whole process of solvent-cast printing, and offer a general guideline for microstructures fabrication. Furthermore, this novel microfabrication approach that uses PLA solutions can be readily extended to other thermoplastic polymers and nanocomposites and enables a broad array of applications including tissue engineering scaffolds (*e.g.*, biocompatible and biodegradable 3D cylindrical meshes for stents), stimuli-responsive materials (*e.g.*, freestanding strain sensors) and microelectronic devices (*e.g.*, micro Ka band helical antenna).

ACKNOWLEDGMENTS

The authors acknowledge the financial support from NSERC (Natural Sciences and Engineering Research Council of Canada) and Canada Research Chair. A scholarship for Mr. Guo was also provided by the China Scholarship Council (CSC).

REFERENCES

1. Lebel, L. L.; Aissa, B.; El Khakani, M. A.; Therriault, D. Ultraviolet-Assisted Direct-Write Fabrication of Carbon Nanotube/Polymer Nanocomposite Microcoils. *Adv. Mater.* **2010,** *22* (5), 592-596.
2. Brown, T. D.; Dalton, P. D.; Hutmacher, D. W. Direct Writing By Way of Melt Electrospinning. *Adv. Mater.* **2011,** *23* (47), 5651-5657.
3. Barry, R. A.; Shepherd, R. F.; Hanson, J. N.; Nuzzo, R. G.; Wiltzius, P.; Lewis, J. A. Direct-Write Assembly of 3D Hydrogel Scaffolds for Guided Cell Growth. *Adv. Mater.* **2009,** *21* (23), 2407-2410.
4. Zheng, J.; Xie, H.; Yu, W.; Tan, M.; Gong, F.; Liu, X.; Wang, F.; Lv, G.; Liu, W.; Zheng, G.; Yang, Y.; Xie, W.; Ma, X. Enhancement of Surface Graft Density of MPEG on Alginate/Chitosan Hydrogel Microcapsules for Protein Repellency. *Langmuir* **2012,** *28* (37), 13261-13273.
5. Gratson, G. M.; García-Santamaría, F.; Lousse, V.; Xu, M.; Fan, S.; Lewis, J. A.; Braun, P. V. Direct-Write Assembly of Three-Dimensional Photonic Crystals: Conversion of Polymer Scaffolds to Silicon Hollow-Woodpile Structures. *Adv. Mater.* **2006,** *18* (4), 461-465.
6. Wu, W.; DeConinck, A.; Lewis, J. A. Omnidirectional Printing of 3D Microvascular Networks. *Adv. Mater.* **2011,** *23* (24), H178-H183.
7. Therriault, D.; Shepherd, R. F.; White, S. R.; Lewis, J. A. Fugitive Inks for Direct-Write Assembly of Three-Dimensional Microvascular Networks. *Adv. Mater.* **2005,** *17* (4), 395-399.
8. Hanson Shepherd, J. N.; Parker, S. T.; Shepherd, R. F.; Gillette, M. U.; Lewis, J. A.; Nuzzo, R. G. 3D Microperiodic Hydrogel Scaffolds for Robust Neuronal Cultures. *Adv. Funct. Mater.* **2011,** *21* (1), 47-54.
9. Karageorgiou, V.; Kaplan, D. Porosity of 3D biomaterial scaffolds and osteogenesis. *Biomaterials* **2005,** *26* (27), 5474-5491.
10. Farahani, R. D.; Dalir, H.; Borgne, V. L.; Gautier, L. A.; Khakani, M. A. E.; Lévesque, M.; Therriault, D. Direct-write fabrication of freestanding nanocomposite strain sensors. *Nanotechnology* **2012,** *23* (8), 085502.
11. Yang, W.; Ratinac, K. R.; Ringer, S. P.; Thordarson, P.; Gooding, J. J.; Braet, F. Carbon Nanomaterials in Biosensors: Should You Use Nanotubes or Graphene? *Angew. Chem. Int. Ed.* **2010,** *49* (12), 2114-2138.
12. Chan, V.; Zorlutuna, P.; Jeong, J. H.; Kong, H.; Bashir, R. Three-dimensional photopatterning of hydrogels using stereolithography for long-term cell encapsulation. *Lab Chip* **2010,** *10* (16), 2062-2070.
13. van Blaaderen, A.; Ruel, R.; Wiltzius, P. Template-directed colloidal crystallization. *Nature* **1997,** *385* (6614), 321-324.
14. Gratson, G. M.; Xu, M.; Lewis, J. A. Microperiodic structures: direct writing of three-dimensional webs. *Nature* **2004,** *428* (6981), 386-386.

15. Therriault, D.; White, S. R.; Lewis, J. A. Chaotic mixing in three-dimensional microvascular networks fabricated by direct-write assembly. *Nat. Mater.* **2003,** *2* (4), 265-271.
16. Lewis, J. A. Direct Ink Writing of 3D Functional Materials. *Adv. Funct. Mater.* **2006,** *16* (17), 2193-2204.
17. Lewis, J. A.; Gratson, G. M. Direct writing in three dimensions. *Mater. Today* **2004,** *7* (7–8), 32-39.
18. Farahani, R. D.; Dalir, H.; Aissa, B.; El Khakani, M. A.; Lévesque, M.; Therriault, D. Micro-infiltration of three-dimensional porous networks with carbon nanotube-based nanocomposite for material design. *Composites, Part A* **2011,** *42* (12), 1910-1919.
19. Lebel, L. L.; Aïssa, B.; Paez, O. A.; Martina, K.; Therriault, D. Three-dimensional micro structured nanocomposite beams by microfluidic infiltration. *J. Micromech. Microeng.* **2009,** *19* (12), 125009.
20. Bruneaux, J.; Therriault, D.; Heuzey, M. C. Micro-extrusion of organic inks for direct-write assembly. *J. Micromech. Microeng.* **2008,** *18* (11), 115020.
21. Smay, J. E.; Gratson, G. M.; Shepherd, R. F.; Cesarano, J.; Lewis, J. A. Directed Colloidal Assembly of 3D Periodic Structures. *Adv. Mater.* **2002,** *14* (18), 1279-1283.
22. Smay, J. E.; Cesarano, J.; Lewis, J. A. Colloidal Inks for Directed Assembly of 3-D Periodic Structures. *Langmuir* **2002,** *18* (14), 5429-5437.
23. Adams, J. J.; Duoss, E. B.; Malkowski, T. F.; Motala, M. J.; Ahn, B. Y.; Nuzzo, R. G.; Bernhard, J. T.; Lewis, J. A. Conformal Printing of Electrically Small Antennas on Three-Dimensional Surfaces. *Adv. Mater.* **2011,** *23* (11), 1335-1340.
24. Gratson, G. M.; Lewis, J. A. Phase Behavior and Rheological Properties of Polyelectrolyte Inks for Direct-Write Assembly. *Langmuir* **2005,** *21* (1), 457-464.
25. Xu, M.; Lewis, J. A. Phase Behavior and Rheological Properties of Polyamine-Rich Complexes for Direct-Write Assembly. *Langmuir* **2007,** *23* (25), 12752-12759.
26. Malda, J.; Visser, J.; Melchels, F. P.; Jüngst, T.; Hennink, W. E.; Dhert, W. J. A.; Groll, J.; Hutmacher, D. W. 25th Anniversary Article: Engineering Hydrogels for Biofabrication. *Adv. Mater.* **2013,** *25* (36), 5011-5028.
27. Melchels, F. P. W.; Domingos, M. A. N.; Klein, T. J.; Malda, J.; Bartolo, P. J.; Hutmacher, D. W. Additive manufacturing of tissues and organs. *Prog. Polym. Sci.* **2012,** *37* (8), 1079-1104.
28. Schuurman, W.; Levett, P. A.; Pot, M. W.; van Weeren, P. R.; Dhert, W. J. A.; Hutmacher, D. W.; Melchels, F. P. W.; Klein, T. J.; Malda, J. Gelatin-Methacrylamide Hydrogels as Potential Biomaterials for Fabrication of Tissue-Engineered Cartilage Constructs. *Macromol. Biosci.* **2013,** *13* (5), 551-561.
29. Drumright, R. E.; Gruber, P. R.; Henton, D. E. Polylactic Acid Technology. *Adv. Mater.* **2000,** *12* (23), 1841-1846.
30. Fambri, L.; Pegoretti, A.; Fenner, R.; Incardona, S. D.; Migliaresi, C. Biodegradable fibres of poly(-lactic acid) produced by melt spinning. *Polymer* **1997,** *38* (1), 79-85.

31. Gupta, B.; Revagade, N.; Hilborn, J. Poly(lactic acid) fiber: An overview. *Prog. Polym. Sci.* **2007,** *32* (4), 455-482.
32. Yamada, A.; Niikura, F.; Ikuta, K. A three-dimensional microfabrication system for biodegradable polymers with high resolution and biocompatibility. *J. Micromech. Microeng.* **2008,** *18* (2), 025035.
33. Berry, S. M.; Warren, S. P.; Hilgart, D. A.; Schworer, A. T.; Pabba, S.; Gobin, A. S.; Cohn, R. W.; Keynton, R. S. Endothelial cell scaffolds generated by 3D direct writing of biodegradable polymer microfibers. *Biomaterials* **2011,** *32* (7), 1872-1879.
34. Vozzi, G.; Flaim, C.; Ahluwalia, A.; Bhatia, S. Fabrication of PLGA scaffolds using soft lithography and microsyringe deposition. *Biomaterials* **2003,** *24* (14), 2533-2540.
35. Guo, S.-Z.; Gosselin, F.; Guerin, N.; Lanouette, A.-M.; Heuzey, M.-C.; Therriault, D. Solvent-Cast Three-Dimensional Printing of Multifunctional Microsystems. *Small* **2013,** *10.1002/smll.201300975, available online 14 Jul 2013.*
36. Gou, Z.; McHugh, A. J. Two-dimensional modeling of dry spinning of polymer fibers. *J. Non-Newtonian Fluid Mech.* **2004,** *118* (2–3), 121-136.
37. Gou, Z.; McHugh, A. J. A comparison of Newtonian and viscoelastic constitutive models for dry spinning of polymer fibers. *J. Appl. Polym. Sci.* **2003,** *87* (13), 2136-2145.
38. Deng, G.; Xia, Q.; Xu, Y.; Zhang, Q. Simulation of dry-spinning process of polyimide fibers. *J. Appl. Polym. Sci.* **2009,** *113* (5), 3059-3067.
39. Kojić, N.; Kojić, A.; Kojić, M. Numerical determination of the solvent diffusion coefficient in a concentrated polymer solution. *Commun. Numer. Meth. Engng.* **2006,** *22* (9), 1003-1013.
40. Naga, N.; Yoshida, Y.; Inui, M.; Noguchi, K.; Murase, S. Crystallization of amorphous poly(lactic acid) induced by organic solvents. *J. Appl. Polym. Sci.* **2011,** *119* (4), 2058-2064.
41. Lim, L. T.; Auras, R.; Rubino, M. Processing technologies for poly(lactic acid). *Prog. Polym. Sci.* **2008,** *33* (8), 820-852.
42. Zhang, J.; Tashiro, K.; Tsuji, H.; Domb, A. J. Disorder-to-Order Phase Transition and Multiple Melting Behavior of Poly(l-lactide) Investigated by Simultaneous Measurements of WAXD and DSC. *Macromolecules* **2008,** *41* (4), 1352-1357.
43. Tsai, C.-C.; Wu, R.-J.; Cheng, H.-Y.; Li, S.-C.; Siao, Y.-Y.; Kong, D.-C.; Jang, G.-W. Crystallinity and dimensional stability of biaxial oriented poly(lactic acid) films. *Polym. Degrad. Stab.* **2010,** *95* (8), 1292-1298.
44. Fischer, E.; Sterzel, H. J.; Wegner, G. Investigation of the structure of solution grown crystals of lactide copolymers by means of chemical reactions. *Colloid Polym. Sci.* **1973,** *251* (11), 980-990.
45. Wang, D.-Y.; Gohs, U.; Kang, N.-J.; Leuteritz, A.; Boldt, R.; Wagenknecht, U.; Heinrich, G. Method for Simultaneously Improving the Thermal Stability and Mechanical Properties of Poly(lactic acid): Effect of High-Energy Electrons on the Morphological, Mechanical, and Thermal Properties of PLA/MMT Nanocomposites. *Langmuir* **2012,** *28* (34), 12601-12608.

TOC Figure

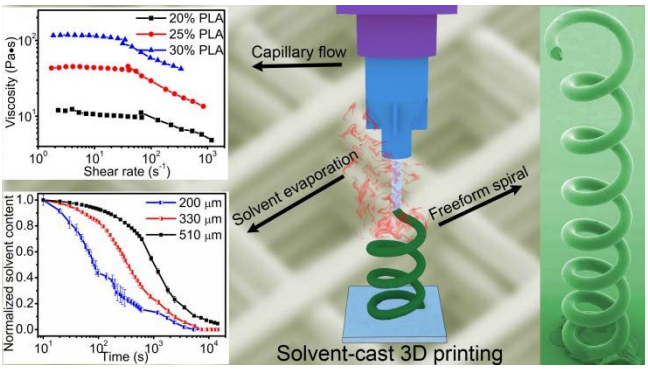
20% PLA
25% PLA
30% PLA
Viscosity (Pa•s)
Shear rate (s⁻¹)
200 μm
330 μm
510 μm
Normalized solvent content
Time (s)
Capillary flow
Solvent evaporation
Freeform spiral
Solvent-cast 3D printing